

# Modulating resistive switching in $\text{Ni}_{0.5}\text{Zn}_{0.5}\text{Fe}_2\text{O}_4$ memristors: The role of manganese doping concentrations

Jiahao Zhang, Xinrong Ren, Yuxin Pan, Yuede Nan, Hui Zheng\*

Laboratory for Nanoelectronics and NanoDevices, Department of Electronics Science and Technology, Hangzhou Dianzi University, Hangzhou, 310018, China

## ARTICLE INFO

Handling editor: Dr P. Vincenzini

**Keywords:**  
Memristors  
Ferrites  
Resistance switch  
Oxygen vacancy  
Electrical

## ABSTRACT

Memristors, recognized as key devices for mitigating the von Neumann bottleneck, show great potential in non-volatile memory technology. Their performance is fundamentally linked to the chemical composition and structural characteristics of their intermediate dielectric layer. Owing to the inherent advantages of metal oxides, such as their simplistic chemical makeup and superior thermal stability, memristors featuring a Metal-Insulator-Metal (MIM) sandwich structure with metal oxides as the intermediate layer have received extensive focus. In this study, a  $\text{Pt}/\text{Ni}_{0.5}\text{Zn}_{0.5}\text{Mn}_x\text{Fe}_{2-x}\text{O}_4(\text{NZMFO})/\text{Pt}$  composite film was prepared, and its resistance switching behavior was modulated by altering the doping concentration of  $\text{Mn}^{n+}$  in NZMFO. The experimental results indicate that altering the  $\text{Mn}^{n+}$  doping concentration does significantly impact the content of oxygen vacancies. As the concentration of  $\text{Mn}^{n+}$  increases from 0.10 to 0.20 at.%, the content of oxygen vacancies correspondingly rises from 46.58 % to 76.42 %. Concurrently, variations in  $\text{Mn}^{n+}$  doping concentration significantly alter the resistance switching properties of the  $\text{Pt}/\text{NZMFO}/\text{Pt}$  composite films. This includes elevating the set/reset voltage, diminishing the resistance ratio, and enhancing the durability with the augmentation of  $\text{Mn}^{n+}$  concentration. By meticulously adjusting the  $\text{Mn}^{n+}$  doping concentration, we can achieve a memristor characterized by superior performance across all metrics. Considering all performance aspects, this study determined that the  $\text{Pt}/\text{NZMFO}/\text{Pt}$  thin film memristor with  $x = 0.15$  exhibits adequate endurance (100 cycles), high data retention, and stable set/reset voltage. This work underscores the critical role of  $\text{Mn}^{n+}$  doping concentration in optimizing the electrochemical properties of NZFO memristors, illustrating a strategic pathway to engineer memristive devices with enhanced performance for future non-volatile memory applications.

## 1. Introduction

Recently, the advancement in the memory industry's manufacturing techniques has approached its technological boundaries. The inability of conventional data storage devices to fulfill the increasing storage demands calls for an immediate exploration of novel memristor variants characterized by swift read/write capabilities, substantial storage capacity, and improved robustness. Memristors are regarded as top contenders in the arena of non-volatile memory solutions and in addressing the von Neumann bottleneck, thanks to their distinct aptitude for merging sensing, storing, and processing functionalities [1–3]. With the progression of information technology, a growing need for storage mediums with augmented attributes, particularly in energy conservation, expandability, and longevity, has emerged. This heightened requirement for advanced storage options underlines the importance of investigating new materials that exhibit enhanced qualities to propel the

innovation in non-volatile memory technologies [4–7]. Furthermore, the evolving landscape of computing technologies places memristors at the forefront of neuromorphic computing systems, where their capacity for endurance, retention, and energy efficiency becomes paramount.

Spinel ferrite, an important multifunctional technical material, finds widespread use in electronic and magnetic devices [8,9]. Spinel ferrites demonstrate an exceptional ability to transfer oxygen and electrons, a characteristic attributed to various vacancies and defects within their structure [10,11]. Concurrently, elemental doping in spinel ferrite reduces formation energy inside and near the grain boundary, facilitating oxygen vacancy formation at doping sites and decreasing the randomness of conductive filament formation, thereby influencing the resistance switching performance of the memory device [12–15]. Various ions ( $\text{Ta}^{n+}$ ,  $\text{Mo}^{n+}$ ,  $\text{Cr}^{n+}$ ) have been doped into spinel ferrite, altering its internal structure characterized by high-density defects [16–18].

Among the doped ions, Mn ion has been particularly applied across

\* Corresponding author.

E-mail address: [zhenghui0551@hdu.edu.cn](mailto:zhenghui0551@hdu.edu.cn) (H. Zheng).

<https://doi.org/10.1016/j.ceramint.2024.04.156>

Received 14 February 2024; Received in revised form 6 April 2024; Accepted 13 April 2024

Available online 15 April 2024

0272-8842/© 2024 Elsevier Ltd and Techna Group S.r.l. All rights reserved.

numerous materials due to its diverse valence states [19–25]. Dai observed that the Mn-doped ferromagnetic amorphous gallium oxide memristors show a high  $R_{\text{off}}/R_{\text{on}}$  ratio of  $10^3$ , at least one order of magnitude higher than those of previously reported purely gallium oxide-based memristors [26]. Xu discovered that Mn doping reduces the band gap of  $\text{SnO}_2$ , potentially forming a conductive path in the cell, thereby expediting the Set and Reset processes in RRAM [27]. Yang noted that Mn-doped  $\text{SrTiO}_3$  thin film memristors can significantly improve the RS performance of device by doping Mn ions into STO to replace part of Ti ions, and helps to explore the cutting-edge applications of high-performance RS devices in information processing and AI [28]. This accumulation of evidence highlights the multifaceted role of Mn doping in modifying the electrical and magnetic properties of various materials. Similarly, in spinel structures, substituting  $\text{Mn}^{n+}$  for  $\text{Fe}^{n+}$  alters the configuration of inherent defects, thereby affecting their electromagnetic properties.  $\text{Mn}^{n+}$  possesses a broader valence state range than  $\text{Fe}^{n+}$ , enabling more effective regulation of electromagnetic properties [29,30]. Consequently, investigating the impact of Mn doping on the resistance switching characteristics of ferrite films is a viable approach.

In this study,  $\text{Ni}_{0.5}\text{Zn}_{0.5}\text{Mn}_x\text{Fe}_{2-x}\text{O}_4$  (NZMFO) ferrite thin films with different Mn doping concentrations were deposited by PLD technology, and different NZMFO thin film memristors were obtained. The study focused on the creation and breaking of conductive filaments of oxygen vacancies within the NZMFO functional layer, revealing that the NZMFO device exhibits characteristics of resistance switching. In addition, the effect of Mn doping concentration on the microstructure of NZMFO thin films and the resistance switching performance of the corresponding devices were studied by using sufficient material characterization. Finally, the effects of oxygen vacancy concentration on the high and low resistance ratio and stability of the corresponding resistive switching devices from 0.10 to 0.20 at.% Mn doping concentration were studied. At the same time, we observed that increasing Mn doping concentration directly correlates with enhanced endurance and retention [31,32]. These findings align with recent studies highlighting the importance of material composition and doping in improving neuromorphic device performance [33,34]. By meticulously adjusting the Mn doping concentration, our study suggests a viable pathway to optimizing RRAM devices for neuromorphic computing applications, offering a strategic balance between electrical performance and device stability.

## 2. Experimental sectional

Initially, NZMFO powders with varying Mn concentrations were synthesized using the sol-gel method. Subsequently, these powders were formed into targets for the deposition of NZMFO ferromagnetic metal oxide thin films on  $\text{Al}_2\text{O}_3$  substrates. This deposition was carried out using the pulsed laser deposition (PLD) technique. Prior to the deposition, the alumina substrates were meticulously cleaned using acetone and alcohol. A platinum (Pt) metal film layer was then applied onto the  $\text{Al}_2\text{O}_3$  substrate as the bottom electrode, employing PLD under specific conditions: a laser power of 300 mJ, a laser repetition rate of 5 Hz, and a vacuum level of  $1 \times 10^{-4}$  Pa. The deposition parameters are detailed in Table 1. Under these conditions, NZMFO thin films with different Mn doping levels were successfully deposited on the Pt/ $\text{Al}_2\text{O}_3$  substrates via

PLD. The process involved controlling the substrate and annealing temperatures at 600 °C and 750 °C, respectively.

The composite film's crystal structure underwent characterization through X-ray diffraction (XRD, Ultima IV, Japan) and Raman scattering spectroscopy (Renishaw, Gloucestershire GL12 7DW, United Kingdom). Field emission scanning electron microscopy (SEM, JSM-7800F, JEOL Ltd, Akishima, Tokyo, Japan) and atomic force microscopy (AFM, JPK) were utilized to examine the surface and cross-sectional morphologies of the films. To ascertain the chemical states of the composite membranes, X-ray photoelectron spectroscopy (XPS, ESCALab250, USA) and electron diffraction spectroscopy (EDS, Bruker Nano GmbH Berlin, Germany) were employed. The retention and durability of Pt/NZMFO/Pt device was assessed using a Keithley 4200 instrument, and variations in HRS/LRS and set/reset voltage data were recorded.

## 3. Results and discussion

### 3.1. Effect of Mn doping on structure and morphology of thin film memristor

Fig. 1(a) displays the structural diagram of the thin film memristor, featuring a Metal-Insulator-Metal (MIM) sandwich structure, which represents the most common configuration in current memristor technology [35]. In this MIM-structured device, inert metal Pt was selected as both the upper and lower metal layers, with NZMFO constituting the central resistive layer. Among these, binary oxides offer significant advantages, including simple chemical composition and superior thermal stability. Fig. 1(b) displays the AFM image of the film's surface. The image reveals a smooth film surface, with a root mean square roughness ( $R_q$ ) of the sample being 0.828 nm. Fig. 1(c) illustrates the SEM and EDS image of the cross section. This image demonstrates a distinct layered structure between the ferrite and the metal layer, with the distribution of Fe and Pt elements mirroring that observed in the SEM cross-section. The Pt metal layer measures ~200 nm in thickness, while the ferrite layer is ~400 nm thick, both of which can be regulated by varying the number of deposition cycles. Fig. 1(d) showcases the EDS mapping image of the film surface. This image indicates uniform doping of the Mn element across the film, with other elements also being evenly distributed throughout. This suggests uniform doping of Mn in NZFO, resulting in a NZMFO film of high uniformity.

Fig. 2(a) depicts the XRD pattern of NZMFO and Pt composite films, with the structural characteristics being analyzed within the range of 2θ angles from 20° to 80° [36]. Disregarding the characteristic peaks of the  $\text{Al}_2\text{O}_3$  substrate and the Pt film, the diffraction patterns reveal strong peaks at (113), (004), (333), and (444), aligning with the  $\text{Ni}_{0.5}\text{Zn}_{0.5}\text{Fe}_2\text{O}_4$  structure as per the standard reference card PDF#52-0278 for pure  $\text{Ni}_{0.5}\text{Zn}_{0.5}\text{Fe}_2\text{O}_4$ . This confirmation underscores the presence of the NZFO phase in the composite films. A notable shift in the primary peak (113), from 35.62° to 35.84° towards higher angles, is observed with an increase in Mn doping concentration. This shift is attributable to the ionic radius of  $\text{Mn}^{n+}$  being smaller than that of  $\text{Fe}^{3+}$ . When  $\text{Mn}^{n+}$  ions substitute  $\text{Fe}^{3+}$  sites within the NZFO lattice, this results in a distortion in the spinel structure, which leads to a decrease in the lattice constant. This finding is significant, indicating that Mn doping introduces a level of strain into the lattice without disrupting the spinel structure of the NZFO.

In Fig. 2(b), the architecture of the NZMFO thin film memristor is graphically represented, highlighting the memristor's layered composition and the spinel crystal structure of the doped NZMFO. The schematic zooms into the lattice arrangement, where  $\text{Mn}^{n+}$  are substituted into the spinel framework, depicted by the transition from  $\text{Fe}^{n+}$  to  $\text{Mn}^{n+}$ . This substitution is engineered to enhance the memristive properties of the device by altering the concentration of oxygen vacancies and the electronic states within the lattice, while maintaining the spinel structure integrity.

The XPS results shown in Fig. 3 reveal the valence states of Fe, O, and

**Table 1**

Deposition conditions of the Pt and NZMFO films.

	Pt	NZMFO
Base pressure	$1 \times 10^{-4}$ Pa	$1 \times 10^{-4}$ Pa
Substrate temperature	300 °C	600 °C
Oxygen pressure	–	0.1 Pa
Laser conditions	300 mJ, 5 Hz	300 mJ, 5 Hz
Film thickness	~200 nm	~400 nm
Mn doping concentration	–	~0.10–0.20 at. %

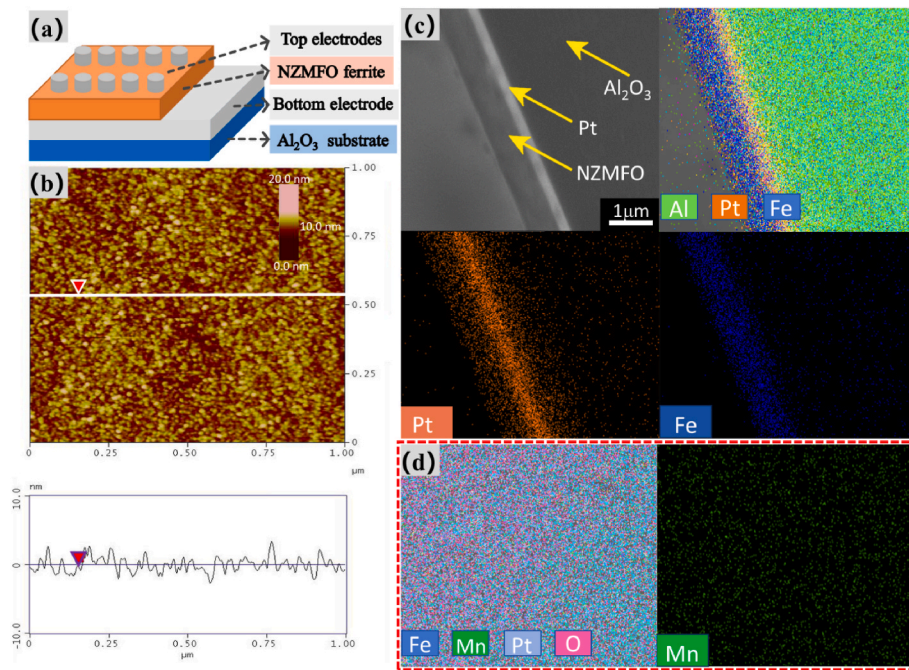


**Fig. 1.** (a) Structural diagram of the thin film memristor, (b) AFM images of the film surface, (c) SEM and EDS images of thin film cross-section, (d) EDS images of the film surface.

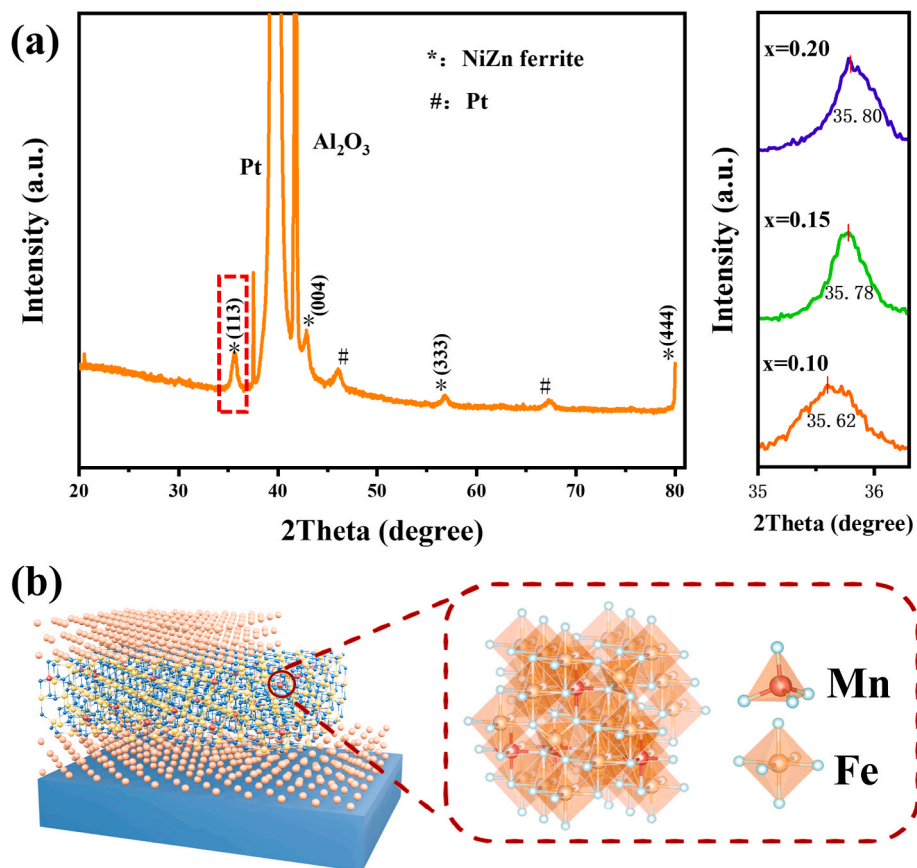


**Fig. 2.** (a) The XRD image of the NZMFO composite film and the comparison of the (113) characteristic peaks at different Mn doping concentrations, (b) The film structure of the NZMFO thin film memristor and the NZMFO spinel crystal structure.



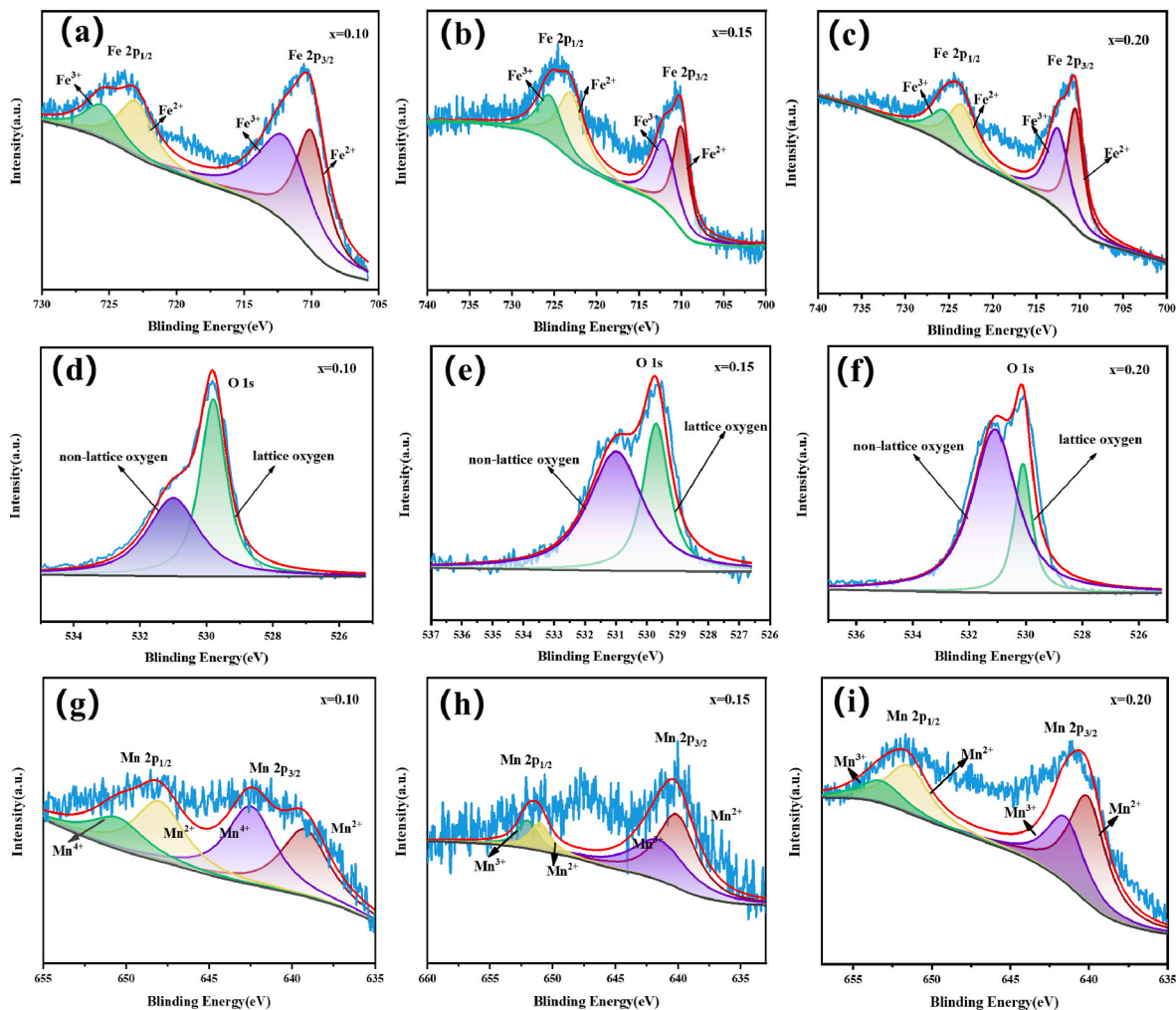


**Fig. 3.** XPS diagrams of Fe elements in thin films with different Mn doping concentrations (a)  $x = 0.10$ , (b)  $x = 0.15$ , (c)  $x = 0.20$ , XPS diagrams of O elements in thin films with different Mn doping concentrations (d)  $x = 0.10$ , (e)  $x = 0.15$ , (f)  $x = 0.20$ , XPS diagram of Mn elements in thin films doped with different concentrations of Mn (g)  $x = 0.10$ , (h)  $x = 0.15$ , (i)  $x = 0.20$ .

Mn in the NZFO thin films, providing insights into their bonding states and oxygen vacancy presence. Fig. 3(a–c) illustrates the Fe 2p spectra, highlighting two iron valence states,  $\text{Fe}^{2+}$  and  $\text{Fe}^{3+}$ . These spectra are separated into two distinct peaks: one indicative of  $\text{Fe}^{2+}$  and the other representing  $\text{Fe}^{3+}$  ions across two lattice sites. In the NZMFO films,  $\text{Fe}^{2+}$  and  $\text{Fe}^{3+}$  exhibit binding energies at 709.9 eV and 711.1 eV, respectively, in the Fe 2p<sub>3/2</sub> state. For the Fe 2p<sub>1/2</sub> state, the peaks corresponding to  $\text{Fe}^{2+}$  and  $\text{Fe}^{3+}$  appear at 723.1 eV and 725.7 eV, respectively.

The appearance of a peak with lower binding energy in the Fe 2p spectra implies the existence of reduced ionic states ( $\text{Fe}^{2+}$ ), which could contribute to the creation of oxygen vacancies in the NZMFO films. Notably, changes in the Fe valence state content are evident when the Mn doping concentrations in these films vary. The quantification of divalent iron content, determined by the ratio  $\text{Fe}^{2+}/(\text{Fe}^{2+} + \text{Fe}^{3+})$ , reveals an increase from 49.6 % to 54.3 %, and then to 55.1 %, with increasing Mn doping concentration, suggesting changes in the oxygen vacancy content.

In the analysis of the O 1s spectra for the NZMFO films, presented in Fig. 3(d–f), two distinct oxygen environments are identified. The peak at the lower binding energy of 529.9 eV is attributed to lattice oxygen, also known as structural oxygen. In contrast, the peak observed at a higher binding energy of 531.3 eV is indicative of non-lattice oxygen, which

may be a contributing factor to oxygen vacancy generation within the active oxide layer. These non-lattice oxygen ions are likely situated at grain boundaries and have the potential to migrate under an applied bias voltage, playing a crucial role in the resistive switching (RS) mechanism [37].

With increasing Mn doping concentration, an increase in the oxygen vacancy content is evident in Fig. 3(d–f). At an  $x$  value of 0.10, the film exhibits both  $\text{Mn}^{2+}$  and  $\text{Mn}^{4+}$  valence states, with corresponding Mn 2p<sub>3/2</sub> binding energies for  $\text{Mn}^{2+}$  and  $\text{Mn}^{4+}$  of 639.2 eV and 642.5 eV, respectively, and their Mn 2p<sub>1/2</sub> XPS peaks located at 648.1 eV and 650.5 eV, respectively. At lower Mn concentrations, the formation of  $\text{MnO}_2$  is enhanced, favoring the existence of  $\text{Mn}^{2+}$  and  $\text{Mn}^{4+}$  states. For  $x = 0.15$ , as illustrated in Fig. 3(h), the film exhibits  $\text{Mn}^{2+}$  and  $\text{Mn}^{3+}$  states with respective Mn 2p<sub>3/2</sub> binding energies of 640.1 eV and 641.5 eV, and Mn 2p<sub>1/2</sub> XPS peaks located at 650.1 eV and 651.8 eV. An increased Mn ion concentration results in the formation of  $\text{Mn}_2\text{O}_3$ , thereby leading to the prevalence of  $\text{Mn}^{2+}$  and  $\text{Mn}^{3+}$  states. Similarly, for  $x = 0.20$ , as shown in Fig. 3(i), the film predominantly displays  $\text{Mn}^{2+}$  and  $\text{Mn}^{3+}$  valence states with respective Mn 2p<sub>3/2</sub> binding energies of 640.1 eV and 641.5 eV, and Mn 2p<sub>1/2</sub> peaks located at 651.5 eV and 653.2 eV. At this increased Mn doping concentration, the formation of  $\text{Mn}_3\text{O}_4$  is suggested, which indicates a general tendency towards the  $\text{Mn}^{2+}$  and  $\text{Mn}^{3+}$  states.



The detected  $\text{Mn}^{2+}$ ,  $\text{Mn}^{3+}$ ,  $\text{Mn}^{4+}$ , and  $\text{Fe}^{2+}$  ions are believed to affect oxygen vacancy formation, as suggested by the fitted peaks at 529.9 eV and 531.3 eV, corresponding to lattice and non-lattice oxygen, respectively. The non-lattice oxygen, which influences the occurrence of oxygen vacancies within the active oxide layer, has the potential to migrate when subjected to an applied bias voltage. In films with varying Mn doping concentrations, oxygen vacancies ( $V_{\text{O}}/(V_{\text{O}}+V_{\text{L}})$ ) are approximately 46.58 %, 62.73 %, 76.42 %, respectively. It is apparent that the content of oxygen vacancies is influenced not only by the divalent iron content but also by the Mn concentration.

### 3.2. Effect of Mn doping on resistance switching characteristics of thin film memristors

The electrical properties of the fabricated Pt/NZMFO/Pt device were subjected to testing. During these evaluations, the top electrode was subjected to a voltage signal in the form of a triangular wave, as exemplified in Fig. 4(d), while the bottom electrode was maintained at ground potential. The I–V curves for Pt/NZMFO/Pt devices with varying Mn doping concentrations are depicted in Fig. 4(a–c). Limiting the current to 10 mA is crucial to preventing device breakdown, followed by using DC scanning to transition the memristor from its initial state to HRS.

As illustrated in Fig. 4(a–c), the current-voltage (I–V) test results on Pt/NZMFO/Pt thin films unequivocally reveal robust bipolar switching characteristics in memristors across three different concentrations. The observation of three symmetric I–V curves indicates effective resistive switching across all three samples. In each case, the films exhibited reversible resistance switching, as denoted by arrows in the figures which indicate the direction of voltage scanning. Upon increasing positive voltage, a rapid increase in current was observed at a voltage termed  $V_{\text{set}}$ , facilitating the device's transition from a high resistance state (HRS) to a low resistance state (LRS) [38,39]. Conversely, the application of a negative voltage, known as  $V_{\text{reset}}$ , led to a sudden drop in current, reverting the device to HRS. As depicted in Fig. 4(e and f), it is noteworthy that as the  $\text{Mn}^{n+}$  concentration increased, both HRS and LRS in the memristors underwent changes, significantly reducing the ratio

between high and low resistance states, while simultaneously increasing the onset voltage. This phenomenon can be attributed to an increase in oxygen vacancy generation at the interface, which leads to a decrease in the Schottky barrier and subsequently reduces the high/low resistance state ratio [40–42]. Upon the application of a positive voltage to the Pt top electrode, oxygen atoms within the NZMFO crystal may undergo oxidation-reduction reactions at the interface adjacent to the top electrode, leading to the formation of oxygen ions. This process results in the emergence of oxygen vacancies at the interface with the Pt top electrode. Consequently, the creation of these oxygen vacancies at the Pt top electrode interface reduces the Schottky barrier potential below that of the interface without oxygen vacancies. Furthermore, the substitution of  $\text{Mn}^{n+}$  for  $\text{Fe}^{n+}$  in NZMFO is hypothesized to degrade the material's overall ferroelectric properties, resulting in weakened internal polarization capabilities, reduced interface polarization charge, and an eventual increase in the onset voltage.

To evaluate the performance of the memristor, tests were conducted on the retention and durability of the Pt/NZMFO/Pt device, as illustrated in Fig. 5. As depicted in Fig. 5(a–c), following the device's switch to HRS or LRS, the sample underwent testing with a readout voltage of 0.1 V per 1 s, yielding a point diagram that demonstrates the data retention of HRS and LRS. The resistance values of HRS and LRS proved to be highly stable, with degradation time extending to  $10^4$  s, suggesting that the device is non-volatile and capable of being read without incurring damage. Following the alteration in Mn doping concentration, no significant change was observed in its retention, implying that Mn doping does not alter the basic structure of the memristor. However, with increased concentration, the ratio of high to low resistance states decreases markedly. In Fig. 5(d–f), the durability of the resistance switching characteristics of Pt/NZMFO/Pt devices was assessed. Following 100 DC cycles, stable resistance switching characteristics were observed, with minimal fluctuation in the resistance of HRS and LRS. Simultaneously, it was clearly evident that the repeatability enhanced significantly as the doping concentration increased. The results indicate that the stability of the resistance switching characteristics reaches its zenith at a Mn doping concentration of  $x = 0.20$ .

To elucidate the transmission mechanism of RS, a typical double

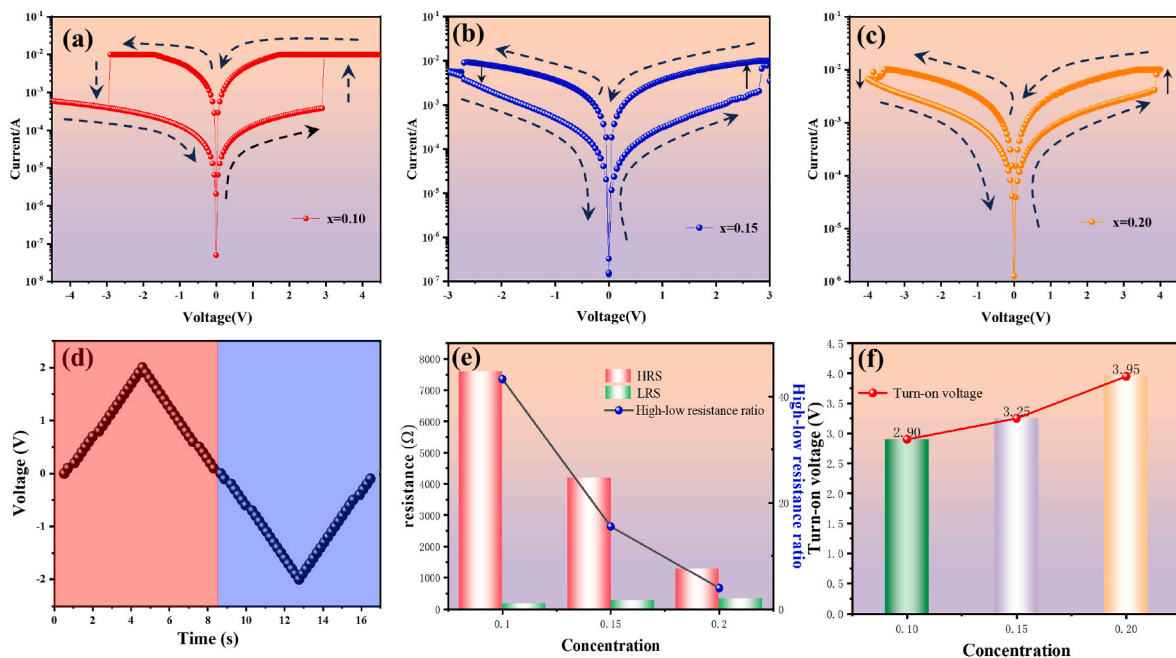


**Fig. 4.** Typical I–V curves of devices with different Mn doping concentrations (a)  $x = 0.10$ , (b)  $x = 0.15$ , (c)  $x = 0.20$ , (d) Triangular wave signal applied to the top electrode, (e) The resistance and high-low resistance ratio of each concentration sample at 0.1 V, (f) The turn-on voltage of each concentration sample.

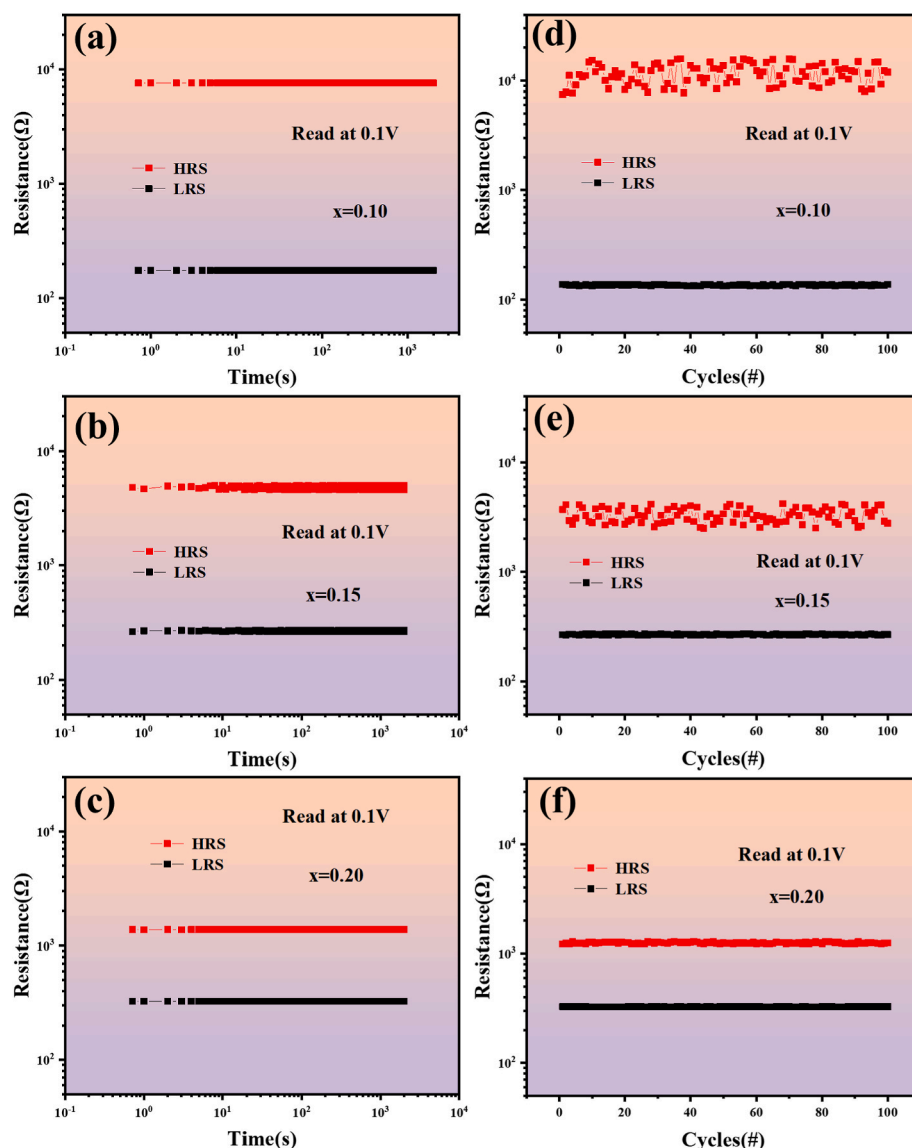


**Fig. 5.** Retention testing of devices with different Mn doping concentrations (a)  $x = 0.10$ , (b)  $x = 0.15$ , (c)  $x = 0.20$ , Repeatability test of devices with different Mn doping concentrations (d)  $x = 0.10$ , (e)  $x = 0.15$ , (f)  $x = 0.20$ .

logarithmic I–V curve was plotted, as illustrated in Fig. 6(a–c). These lines represent the fitting results for each data point. Clearly, irrespective of the Mn doping concentration in the NZFO film, the I–V curve for the LRS state exhibits a linear plot with a slope of approximately 1, suggesting that Ohm's law predominates the conduction mechanism in the LRS. However, the I–V characteristic curve of the HRS state in the low voltage region also presents linear fitting results, with a slope of approximately 1, implying that the low voltage region of the HRS is equally governed by Ohm's law. The behavior in the high voltage region exhibits a non-linear relationship, clearly indicating a distinct conductive mechanism. Analysis was conducted using the Schottky emission mechanism, Poole-Frenkel emission mechanism, and SCLC mechanism, as demonstrated in Fig. 6(g–i). Upon comparing the confidence coefficient (COD) and conducting further analysis, it is revealed that a more suitable linear relationship exists between  $\ln(I)$  and  $\sqrt{V}$ , as depicted in Fig. 6(d–f), suggesting that Schottky emission predominates as the

main conduction mechanism in the higher voltage region of HRS [43, 44].

In this study, it is plausible that oxygen vacancies accumulate at the grain boundaries of the thin films, with the potential for conductive filaments to form around Mn doping sites at these locations. However, with increasing doping concentration, the device's transition from the High Resistance State (HRS) to the Low Resistance State (LRS) during setting and resetting processes becomes more facile. This phenomenon can be attributed to the high Mn content, potentially encouraging oxygen vacancy accumulation at the grain boundaries, especially around Mn doping sites, thus facilitating conductive filament formation [27, 45]. An abundance of oxygen vacancies renders the film more conductive, resulting in decreased resistance of the HRS under similar conditions and subsequently lowering the high/low resistance state ratio. During the transition from LRS to HRS, the excessive generation of  $\text{Ni}^0$ ,  $\text{Zn}^0$ , and  $\text{Fe}^{2+}$  ions may lead to a marked reduction in oxygen vacancies

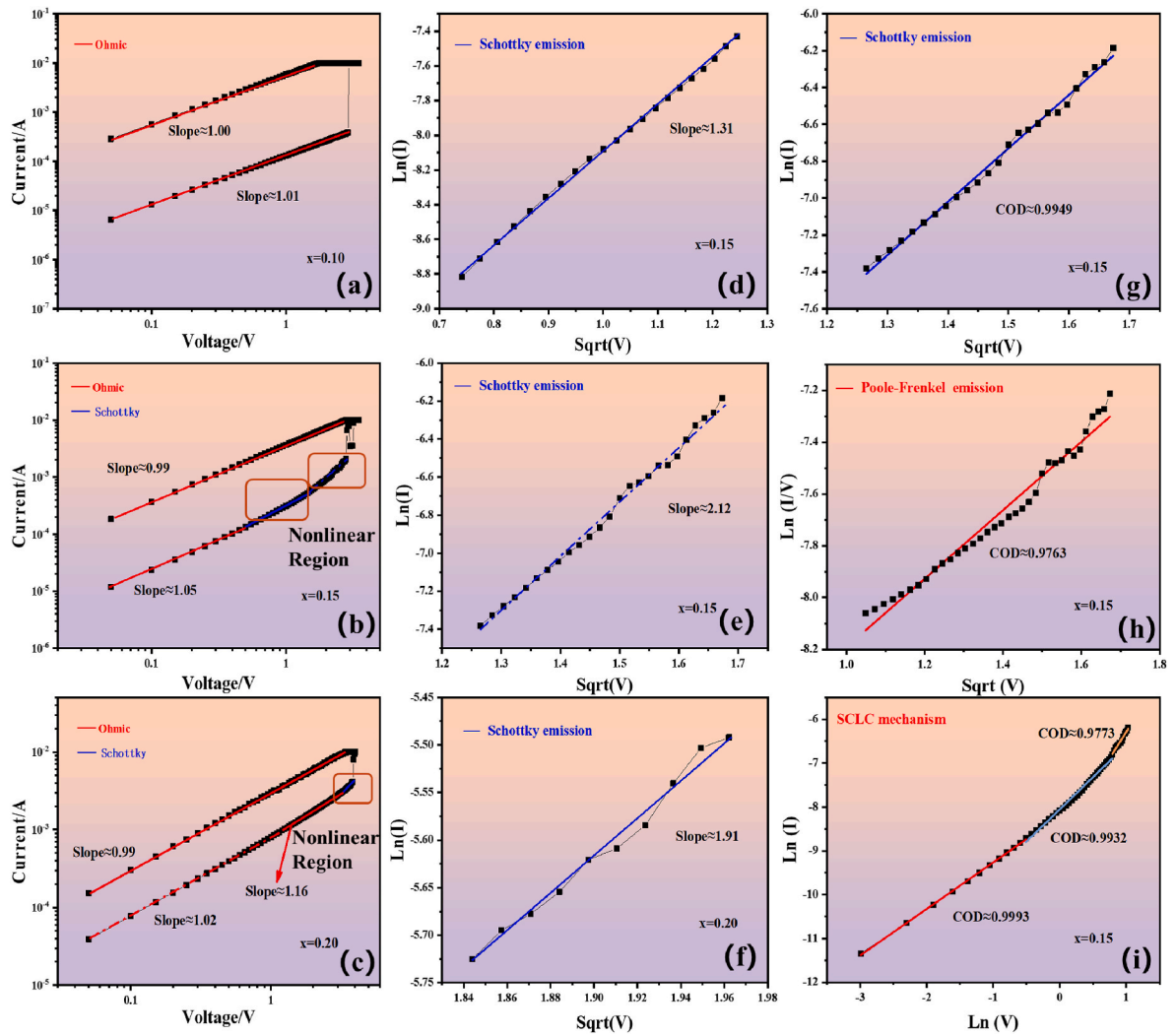


**Fig. 6.**  $I$ - $V$  test curves of devices with different Mn doping concentrations at double logarithmic scale (a)  $x = 0.10$ , (b)  $x = 0.15$ , (c)  $x = 0.20$ , And typical  $\ln(I)$  and  $\sqrt{V}$  diagrams (d) the first half of  $x = 0.15$ , (e) the second half of  $x = 0.15$ , (f)  $x = 0.20$ , The fitting curves of three possible conduction mechanisms in the case of HRS when  $x = 0.15$ , (g) Schottky emission, (h) Poole-Frenkel emission, (i) SCLC mechanism.

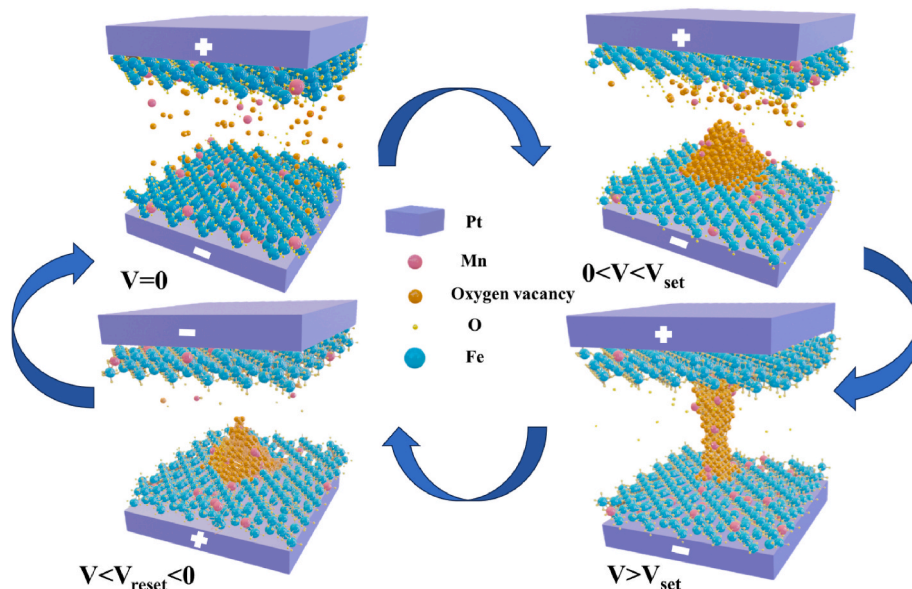


**Fig. 7.** A schematic diagram of the formation/rupture mechanism of conductive filaments in the HRS and LRS states of the NZMFO memristor during the first cycle.



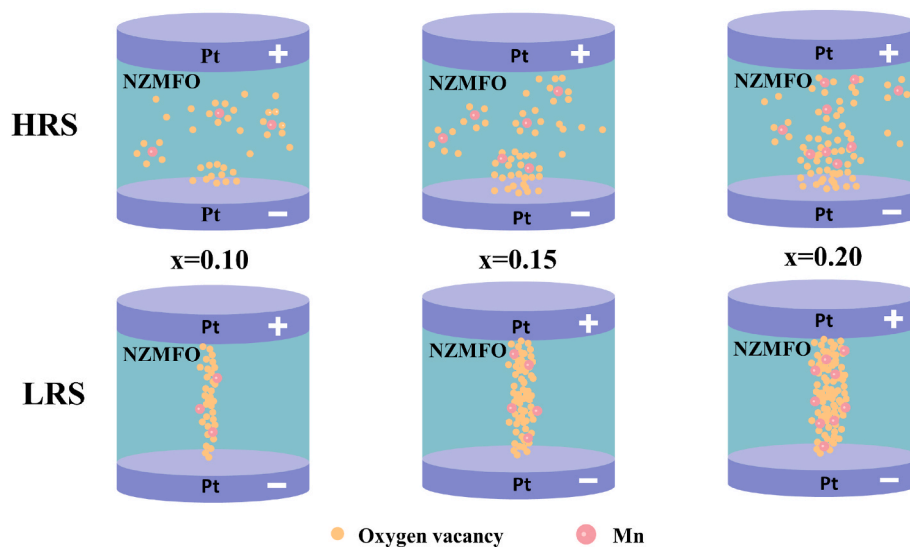


Fig. 8. The mechanism diagram of the effect of different doping concentrations of  $\text{Mn}^{n+}$  on the formation of conductive filaments in NZMFO.

and a decrease in the reset voltage, as illustrated in the I–V curve in Fig. 6(d). Consequently, an increase in  $\text{Mn}^{n+}$  doping concentration accelerates the formation and breakage of conductive filaments, thereby enhancing their stability at the formation sites. Additionally, the increased  $\text{Mn}^{n+}$  doping concentration results in a narrowing of the resistive switching window between high and low resistance states, thus making the switching process more facile and random.

To enhance comprehension of the RS characteristics, a schematic diagram of the formation and fracture of the conduction path during the first cycle of the NZMFO memristor is presented in Fig. 7. Without a bias voltage, oxygen vacancies are randomly dispersed throughout NZMFO. Upon applying a positive voltage to the Pt top electrode, the oxygen vacancies that are generated accumulate near the Pt bottom electrode, driven by the electric field, and subsequently expand in a conical fashion towards the Pt top electrode to form a local conductive filament [46]. Connection of the oxygen vacancy to the top Pt electrode results in the formation of a local oxygen vacancy conductive wire, bridging the upper and lower electrodes and shifting the device resistance from HRS to LRS, marking the Set process. Application of a reverse voltage to the top Pt electrode causes the oxygen within this electrode to interact with the oxygen vacancies at the interface, driven by the electric field. This interaction disrupts the conductive filament, prompting the relocation of oxygen vacancies from the bottom to the top Pt electrode, thereby transitioning the device from a low-resistance to a high-resistance state, culminating in the Reset process [47,48]. Fig. 8 demonstrates that oxygen vacancies are preferentially adsorbed around  $\text{Mn}^{n+}$  ions. An increase in Mn doping concentration leads to a continuous rise in the number of oxygen vacancies, a portion of which accumulates near the bottom Pt electrode due to the influence of the electric field. The greater the number of oxygen vacancies, the more facile the formation of conductive filaments, facilitating the transition of the resistance state from HRS to LRS. In the Set process, the formation of local conductive filaments is facilitated around  $\text{Mn}^{n+}$  ions, accompanied by an increase in  $\text{Ni}^0$ ,  $\text{Zn}^0$ , and  $\text{Fe}^{2+}$ , which accelerates and stabilizes conductive filament formation. During the Reset process, the valence states of  $\text{Ni}^0$ ,  $\text{Zn}^0$ , and  $\text{Fe}^{2+}$  revert to  $\text{Ni}^+$ ,  $\text{Zn}^{2+}$ , and  $\text{Fe}^{3+}$ , respectively, a transition that is

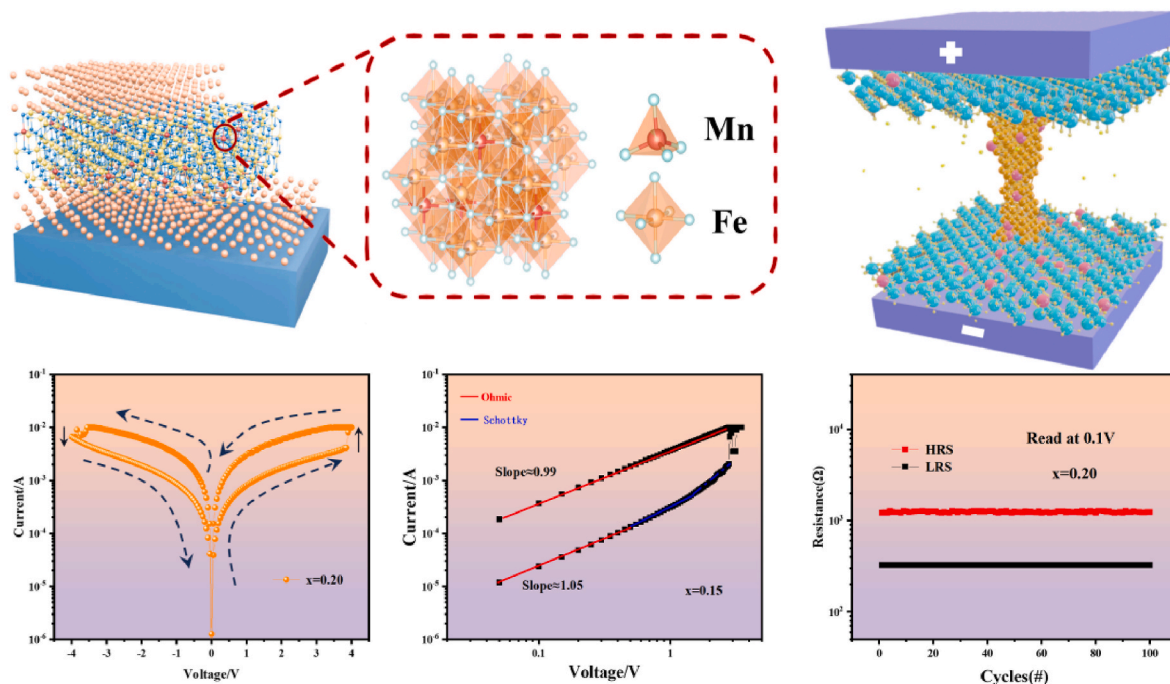
expedited by the reduction of oxygen vacancies upon disconnection of the conductive filament. Consequently, an increased  $\text{Mn}^{n+}$  doping concentration hastens the formation and rupture of conductive filaments, facilitating the swift transition between high and low resistance states and enhancing randomness.

#### 4. Conclusions

This study involved the preparation of NZMFO thin films with varying concentrations of Mn ion doping using PLD (Pulsed Laser Deposition) technology. Structural characterization revealed that Mn ion doping does significantly alter the concentration of oxygen vacancies in the samples. Concurrently, I–V measurements indicated that the NZMFO thin film memristor with a Mn substitution level of  $x = 0.15$  exhibits commendable endurance (100 cycles), superior data retention, and stable setting/reset voltages. Research has demonstrated that Mn doping is crucial in the generation and distribution of oxygen vacancies, with optimal Mn doping enhancing the resistance switching behavior. Thus, incorporating an optimal quantity of Mn into the ferrite can augment the stability and retention capabilities of the resistance switch. It has been established that the performance of memristors can be enhanced through metal ion doping, enabling the preparation of high-performance thin-film memristors. In light of the evolving applications of RRAM devices beyond traditional memory storage, their potential in neuromorphic computing systems has garnered significant interest. Neuromorphic devices, which mimic neural network architectures, require optimized performance characteristics, including inference capabilities, endurance, and data retention, to function effectively. Our investigation into Mn-doped NZMFO memristors reveals significant implications for these performance metrics.

#### Data availability

The datasets generated during and/or analyzed during the current study are available from the corresponding author on request.



### CRediT authorship contribution statement

**Jiahao Zhang:** Data curation, Investigation, Writing – original draft.  
**Xinrong Ren:** Data curation, Visualization, Writing – original draft.  
**Yuxin Pan:** Investigation. **Yuede Nan:** Data curation. **Hui Zheng:** Writing – original draft, Writing – review & editing.

### Declaration of competing interest

The authors declare that they have no known competing financial interests or personal relationships that could have appeared to influence the work reported in this paper.

### Acknowledgments

This work is funded by the National College Students' innovation and entrepreneurship training program (No. 202310336060), the Fundamental Research Funds for the Provincial Universities of Zhejiang (GK239909299001-402), the National Natural Science Foundation of China (Grant No. 51702075).

### References

- [1] S. Choi, J. Yang, G. Wang, Emerging memristive artificial synapses and neurons for energy-efficient neuromorphic computing, *Adv. Mater.* 32 (51) (2020) 2004659.
- [2] C.S. Hwang, Prospective of semiconductor memory devices: from memory system to materials, *Adv. Electron. Mater.* 1 (6) (2015) 1400056.
- [3] D.B. Strukov, G.S. Snider, D.R. Stewart, R.S. Williams, The missing memristor found (vol 453, pg 80, 2008), *Nature* 459 (7250) (2009) 80–83.
- [4] M.W. Si, H.Y. Cheng, T. Ando, G.H. Hu, P.D. Ye, Overview and outlook of emerging non-volatile memories, *MRS Bull.* 46 (10) (2021) 946–958.
- [5] M.A. Zidan, J.P. Strachan, W.D. Lu, The future of electronics based on memristive systems, *Nat. Electron.* 1 (1) (2018) 22–29.
- [6] B. Hwang, J.S. Lee, Recent advances in memory devices with hybrid materials, *Adv. Electron. Mater.* 5 (1) (2019) 1800519.
- [7] S. Gao, X.H. Yi, J. Shang, G. Liu, R.W. Li, Organic and hybrid resistive switching materials and devices, *Chem. Soc. Rev.* 48 (6) (2019) 1531–1565.
- [8] S.B. Narang, K. Pubby, Nickel spinel ferrites: a review, *J. Magn. Magn. Mater.* 519 (2021) 167163.
- [9] M.A. Darwish, S.A. Saafan, D. El-Kony, N.A. Salahuddin, Preparation and investigation of dc conductivity and relative permeability of epoxy/Li-Ni-Zn ferrite composites, *J. Magn. Magn. Mater.* 385 (2015) 99–106.
- [10] H. Qin, Y.Z. He, P.A. Xu, D.L. Huang, Z.W. Wang, H. Wang, Z.X. Wang, Y. Zhao, Q. Y. Tian, C.L. Wang, Spinel ferrites (MFe<sub>2</sub>O<sub>4</sub>): synthesis, improvement and catalytic application in environment and energy field, *Adv. Colloid Interface Sci.* 294 (2021) 102486.
- [11] A. Hajalilou, H.M. Kamari, K. Shamel, Dielectric and electrical characteristics of mechanically synthesized Ni-Zn ferrite nanoparticles, *J. Alloys Compd.* 708 (2021) 813–826.
- [12] S.J. Salih, W.M. Mahmood, Review on magnetic spinel ferrite (MFe<sub>2</sub>O<sub>4</sub>) nanoparticles: from synthesis to application, *Heliyon* 9 (6) (2023) e16601.
- [13] M.D. Hossain, M.A. Hossain, S.S. Sikder, Hysteresis loop properties of rare earth doped spinel ferrites: a review, *J. Magn. Magn. Mater.* 564 (2022) 170095.
- [14] X.F. Niu, C.C. Liu, B.F. Zong, Investigation on the microstructure and magnetic properties of Mg(Ga<sub>2-x</sub>Fe<sub>x</sub>)O<sub>4</sub> spinel ferrites, *J. Mater. Sci. Mater. Electron.* 34 (2) (2023) 118.
- [15] G.H. Bai, W.J. Zhong, Z.H. Zhang, S. Bandaru, X.Y. Fan, X.L. Liu, X.F. Zhang, Atomic-scale observation of calcium occupation in spinel cobalt ferrite towards the regulation of intrinsic magnetic properties, *Nanoscale* 15 (48) (2023) 19586–19597.
- [16] S. Tominc, A. Recnik, S. Bernik, M. Mazaj, N. Daneu, Charge compensation and electrical characteristics of Ta<sub>2</sub>O<sub>5</sub>-doped SnO<sub>2</sub>-CoO ceramics, *J. Eur. Ceram. Soc.* 40 (2) (2020) 355–361.
- [17] A.K. Pradhan, S. Saha, T.K. Nath, AC and DC electrical conductivity, dielectric and magnetic properties of Co<sub>0.65</sub>Zn<sub>0.35</sub>Fe<sub>2-x</sub>Mo<sub>x</sub>O<sub>4</sub> (x=0.0, 0.1 and 0.2) ferrites, *Appl. Phys. Mater. Sci. Process* 123 (11) (2017) 1–8.
- [18] L.C. Xue, L.L. Lang, J. Xu, Z.Z. Li, W.H. Qi, G.D. Tang, L.Q. Wu, Magnetic moment directions and distributions of cations in Cr (Co) substituted spinel ferrites Ni<sub>0.7</sub>Fe<sub>2.3</sub>O<sub>4</sub>, *AIP Adv.* 5 (9) (2015).
- [19] Y. Li, M.Y. Bian, N.N. Zhang, W. Bai, J. Yang, Y.Y. Zhang, X.D. Tang, J.H. Chu, Mn-doping composition dependence of the structures, electrical and magnetic properties, and domain structure/switching of Aurivillius Bi<sub>5</sub>Ti<sub>3</sub>FeO<sub>15</sub> films, *Ceram. Int.* 45 (7) (2019) 8634–8639.
- [20] W.J. Mir, A. Swarnkar, A. Nag, Postsynthesis Mn-doping in CsPbI<sub>3</sub> nanocrystals to stabilize the black perovskite phase, *Nanoscale* 11 (10) (2019) 4278–4286.
- [21] A.K. Guria, S.K. Dutta, S. Das Adhikari, N. Pradhan, Doping Mn<sup>2+</sup> in lead Halide perovskite nanocrystals: successes and challenges, *ACS Energy Lett.* 2 (5) (2017) 1014–1021.
- [22] Z.Y. Wu, F. Ye, Q. Liu, R. Pang, Y. Liu, L. Jiang, Z.L. Tang, L.F. Hu, Simultaneous incorporation of V and Mn element into polyanionic NASICON for high energy-density and long-lifespan Zn-ion storage, *Adv. Energy Mater.* 12 (23) (2022) 2200654.
- [23] J.Y. Cao, J.J. Li, W. Chu, W.L. Cen, Facile synthesis of Mn-doped BiOI for metronidazole photodegradation: optimization, degradation pathway, and mechanism, *Chem. Eng. J.* 400 (2020) 125813.
- [24] J. Liang, Z.H. Liu, L.J. Qiu, Z. Hawash, L.Q. Meng, Z.F. Wu, Y. Jiang, L.K. Ono, Y. B. Qi, Enhancing optical, electronic, crystalline, and morphological properties of cesium lead Halide by Mn substitution for high-stability all-inorganic perovskite solar cells with carbon electrodes, *Adv. Energy Mater.* 8 (20) (2018) 1800504.
- [25] W.Y. Liu, Q.L. Lin, H.B. Li, K.F. Wu, I. Robel, J.M. Pietryga, V.I. Klimov, Mn<sup>2+</sup>-Doped lead Halide perovskite nanocrystals with dual-color emission controlled by Halide content, *J. Am. Chem. Soc.* 138 (45) (2016) 14954–14961.

- [26] X. Dai, X. Zhang, D. Gong, G. Xiang, Performance enhancement and in situ observation of resistive switching and magnetic modulation by a tunable two-level system of Mn dopants in  $\alpha$ -gallium oxide-based memristor, *Adv. Funct. Mater.* 33 (49) (2023) 2304749.
- [27] Z.M. Xu, T.H. Ji, S.L. Zhang, P.Y. Guan, J. Elliott, T. Wan, C. Cazorla, D.W. Chu, The cationic interstitials induced resistive switching: a case study on Mn-doped  $\text{SnO}_2$ , *Mater. Sci. Technol.* 39 (10) (2023) 1180–1186.
- [28] Y.S. Yang, B. Sun, G.D. Zhou, C. Ke, J. Zhang, Y.Z. Zhou, S.S. Mao, J.J. Qin, Y. Zhao, Improved resistive switching performance and in-depth mechanism analysis in Mn-doped  $\text{SrTiO}_3$ -based RRAM, *Mater. Today Commun.* 35 (2023) 105512.
- [29] R. Sharma, P. Thakur, M. Kumar, P.B. Barman, P. Sharma, V. Sharma, Enhancement in A-B super-exchange interaction with  $\text{Mn}^{2+}$  substitution in Mg-Zn ferrites as a heating source in hyperthermia applications, *Ceram. Int.* 43 (16) (2017) 13661–13669.
- [30] J. Xu, L. Ma, Z.Z. Li, L.L. Lang, W.H. Qi, G.D. Tang, L.Q. Wu, L.C. Xue, G.H. Wu, Antiferromagnetic coupling between  $\text{Mn}^{3+}$  and  $\text{Mn}^{2+}$  cations in Mn-doped spinel ferrites, *Phys. Status Solidi B* 252 (12) (2015) 2820–2829.
- [31] C.P. Singh, V.P. Singh, H. Ranjan, S.K. Pandey, Bipolar and rectifying resistive switching dynamics in E-beam evaporated  $\text{SnO}_x$  based memristor, *Ceram. Int.* 50 (2) (2024) 4092–4100.
- [32] V.P. Singh, C.P. Singh, H. Ranjan, S.K. Pandey, Investigation of analog resistive switching in solution-processed lead-free perovskite  $\text{Cs}_2\text{SnI}_6$  memristor for synaptic application, *IEEE Trans. Electron. Dev.* 70 (10) (2023) 5092–5098.
- [33] V.P. Singh, C.P. Singh, H. Ranjan, S.K. Pandey, Investigation of analog resistive switching dynamics in microwave-assisted  $\text{Fe}_3\text{O}_4$  based memristor for neuromorphic application, *Mater. Lett.* 344 (2023) 134431.
- [34] C.P. Singh, V.P. Singh, H. Ranjan, S.K. Pandey, Investigation of resistive switching dynamics in e-beam evaporated P-type tin-oxide based cross-cell memristor for synaptic and memory application, *Mater. Lett.* 352 (2023) 135156.
- [35] S. Yu, Neuro-inspired computing with emerging nonvolatile memorys, *Proc. IEEE* 106 (2) (2018) 260–285.
- [36] V.P. Singh, C.P. Singh, H. Ranjan, S.K. Pandey, Experimental demonstration and analysis of crossbar array memristor for brain-inspired computing, *Appl. Mater. Today* 36 (2024) 102045.
- [37] A.Z. Hao, M. Ismail, S. He, N. Qin, R.Q. Chen, A.M. Rana, D.H. Bao, Enhanced resistive switching and magnetic properties of Gd-doped  $\text{NiFe}_2\text{O}_4$  thin films prepared by chemical solution deposition method, *Mater. Sci. Eng. B-Adv. Funct. Solid-State Mater.* 229 (2018) 86–95.
- [38] E.J. Yoo, M. Lyu, J.H. Yun, C.J. Kang, Y.J. Choi, L. Wang, Resistive switching behavior in organic-inorganic hybrid  $\text{CH}_3\text{NH}_3\text{PbI}_{3-x}\text{Cl}_x$  perovskite for resistive random access memory devices, *Adv. Mater.* 27 (40) (2015) 6170–6175.
- [39] S. Yamamoto, T. Kitanaka, T. Miyashita, M. Mitsuishi, Resistive switching of organic-inorganic hybrid devices of conductive polymer and permeable ultra-thin  $\text{SiO}_2$  films, *Nanotechnology* 29 (26) (2018) 26LT02.
- [40] J. Li, Y. Ji, R. Pan, R. Zhao, Y. Yuan, W. Li, H. Yang, Fowler-Nordheim tunneling in  $\beta$ - $\text{Ga}_2\text{O}_3/\text{SrRuO}_3$  Schottky interfaces, *J. Phys. Appl. Phys.* 55 (21) (2022) 210003.
- [41] P. Reddy, D. Khachariya, W. Mecouch, M.H. Breckenridge, P. Bagheri, Y. Guan, J. H. Kim, S. Pavlidis, R. Kirste, S. Mita, E. Kohn, R. Collazo, Z. Sitar, Study on avalanche breakdown and Poole-Frenkel emission in Al-rich AlGaIn grown on single crystal AlN, *Appl. Phys. Lett.* 119 (18) (2021).
- [42] K.H. Xue, B. Traoré, P. Blaise, L.R.C. Fonseca, E. Vianello, G. Molas, B. De Salvo, G. Ghibaudo, B. Magyari-Köpe, Y. Nishi, A combined *Ab initio* and experimental study on the nature of conductive filaments in Pt/HfO<sub>2</sub>/Pt resistive random access memory, *IEEE Trans. Electron. Dev.* 61 (5) (2014) 1394–1402.
- [43] L.X. Zhang, B. Xie, W. Chen, L.N. Fan, H. Zheng, Q. Wu, P. Zheng, L. Zheng, Y. Zhang, Resistive switching behaviours of Pt/Ni<sub>0.5</sub>Zn<sub>0.5</sub>Fe<sub>2</sub>O<sub>4</sub>/Pt based on film thickness for memristor applications, *Ceram. Int.* 49 (2) (2023) 2991–2997.
- [44] Z.A. Jian, S. Mohanty, E. Ahmadi, Temperature-dependent current-voltage characteristics of  $\beta$ - $\text{Ga}_2\text{O}_3$  trench Schottky barrier diodes, *Appl. Phys. Lett.* 116 (15) (2020).
- [45] Y.R. Huang, X.L. Lin, B. Chen, H.D. Zheng, Z.R. Chen, H.H. Li, S.T. Zheng, Thermal-responsive polyoxometalate-metalloviologen hybrid: reversible intermolecular three-component reaction and temperature-regulated resistive switching behaviors, *Angew. Chem. Int. Ed.* 60 (31) (2021) 16911–16916.
- [46] B. Traore, P. Blaise, B. Sklénard, E. Vianello, B. Magyari-Köpe, Y. Nishi, HfO<sub>2</sub>/Ti interface mediated conductive filament formation in RRAM: an *Ab initio* study, *IEEE Trans. Electron. Dev.* 65 (2) (2018) 507–513.
- [47] R. Zhang, H. Huang, Q. Xia, C. Ye, X. Wei, J. Wang, L. Zhang, L.Q. Zhu, Role of oxygen vacancies at the TiO<sub>2</sub>/HfO<sub>2</sub> interface in flexible oxide-based resistive switching memory, *Adv. Electron. Mater.* 5 (5) (2019) 1800833.
- [48] X. Yan, C. Qin, C. Lu, J. Zhao, R. Zhao, D. Ren, Z. Zhou, H. Wang, J. Wang, L. Zhang, Robust Ag/ZrO<sub>2</sub>/WS<sub>2</sub>/Pt memristor for neuromorphic computing, *ACS Appl. Mater. Interfaces* 11 (51) (2019) 48029–48038.